ACS Photonics

Article

pubs.acs.org/journal/apchd5

Electron Dynamics in Silicon–Germanium Terahertz Quantum Fountain Structures

Diego Sabbagh,[†] Johannes Schmidt,[‡,§] Stephan Winnerl,[‡] Manfred Helm,[‡,§] Luciana Di Gaspare,[†] Monica De Seta,[†] Michele Virgilio,[∥] and Michele Ortolani*[,⊥]

[†]Dipartimento di Scienze, Università Roma Tre, Viale Marconi 446, 00146 Rome, Italy

[‡]Institute of Ion Beam Physics and Materials Research "Helmholtz-Zentrum Dresden-Rossendorf", 01314 Dresden, Germany

[§]Institut für Angewandte Physik, TU Dresden, 01062 Dresden, Germany

[∥]Dipartimento di Fisica "E. Fermi", Università di Pisa, Largo Pontecorvo 3, 56127, Pisa, Italy

[⊥]Dipartimento di Fisica, Università di Roma "La Sapienza", Piazzale A. Moro 2, 00185 Rome, Italy

Supporting Information

ABSTRACT: Asymmetric quantum well systems are excellent candidates to realize semiconductor light emitters at far-infrared wavelengths not covered by other gain media. Group-IV semiconductor heterostructures can be grown on silicon substrates, and their dipole-active intersubband transitions could be used to generate light from devices integrated with silicon electronic circuits. Here, we have realized an optically pumped emitter structure based on a three-level Ge/$Si_{0.18}Ge_{0.82}$ asymmetric coupled quantum well design. Optical pumping was performed with a tunable free-electron laser emitting at photon energies of 25 and 41 meV, corresponding to the energies of the first two intersubband transitions 0 → 1 and 0 → 2 as measured by Fourier-transform spectroscopy. We have studied with a synchronized terahertz time-domain spectroscopy probe the relaxation dynamics after pumping, and we have interpreted the resulting relaxation times (in the range 60 to 110 ps) in the framework of an out-of-equilibrium model of the intersubband electron–phonon dynamics. The spectral changes in the probe pulse transmitted at pump–probe coincidence were monitored in the range 0.7–2.9 THz for different samples and pump intensity and showed indication of both free carrier absorption increase and bleaching of the 1 → 2 transition. The quantification from data and models of the free carrier losses and of the bleaching efficiency allowed us to predict the conditions for population inversion and to determine a threshold pump power density for lasing around 500 kW/cm^2 in our device. The ensemble of our results shows that optical pumping of germanium quantum wells is a promising route toward silicon-integrated far-infrared emitters.

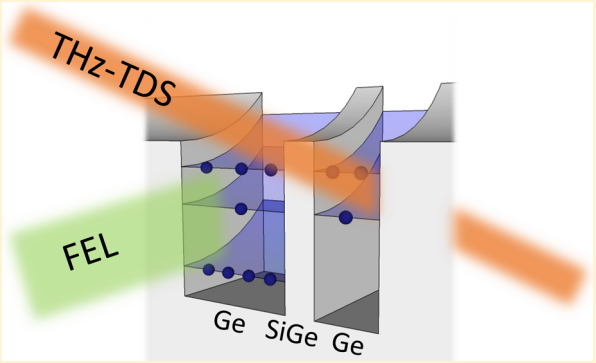

KEYWORDS: *silicon photonics, quantum wells, chemical vapor deposition, terahertz spectroscopy, pump–probe spectroscopy, germanium*

Dipole-active transitions between electron energy levels in quantum wells (QWs) obtained in semiconductor heterostructures have clearly demonstrated their potential for infrared light emission.[1−5] Each level in a QW is constituted by a two-dimensional electron energy subband, and therefore, these transitions are named intersubband (ISB) transitions. One important property of ISB light emitters is that they are unipolar devices, i.e., they do not require the use of semiconductors with a direct bandgap because either electrons or holes are involved in the emission process, and the radiative decay rate does not depend on electron–hole recombination. This property makes ISB transition design a viable route for realizing silicon-based monolithic light emitters, employing silicon-compatible group-IV semiconductor materials with indirect bandgap such as germanium and tin.[6−18] Light emitters realized on silicon wafers could be integrated in the CMOS technology platform[9,16−18] and thus, even if working at low temperatures and in the far-infrared range,[6,7] have the potential to open the field of silicon photonics beyond the telecom technology to applications like chemical sensing, wireless data exchange, and imaging.[4,9] After the first demonstration in 1994 of the quantum cascade laser (QCL),[19] coherent ISB emitters based on electron injection-tunneling between coupled QWs[20] are now an established technology, although QCLs in group-IV semiconductors could not be realized so far.[5] Concerning optically pumped ISB devices, the ISB Raman laser based on virtual excited states was demonstrated in 2001,[21] but they were realized only in group III–V semiconductor compounds.[22−25] In group-IV semiconductors, the ISB Raman laser is difficult to

Received: September 30, 2015
Published: February 1, 2016

DOI: 10.1021/acsphotonics.5b00561
ACS Photonics 2016, 3, 403−414

realize due to the lack of polar optical phonons for the Raman Stokes process.[24] More recently, sources based on difference-frequency generation were realized but still only in III−V compounds.[26] At the cost of higher losses but with the potential for higher gain,[27,28] one can also design and realize three-level ISB emitters that exploit transitions between real excited states (so-called "quantum fountain" device).[29−35] Design of quantum fountain lasers in group-IV materials was seldom reported,[36] and it is the subject of the present work. In these devices, the electrons are optically pumped from the fundamental subband (level 0), populated by substitutional doping, to the third subband (level 2) in order to allow the light emission resulting from the radiative transition to move toward the almost unoccupied second subband (level 1). Electrons can then relax back to the fundamental level 0, hence depopulating level 1 and allowing further transitions from level 2, as depicted in Figure 1. Establishment of this loop process does not

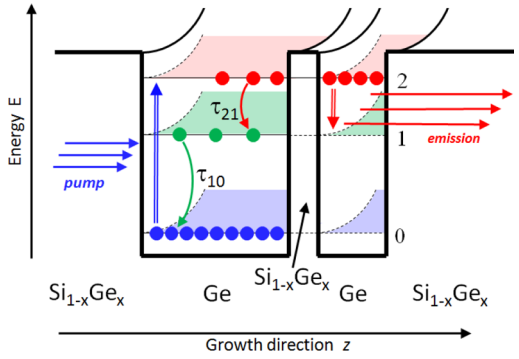

Figure 1. Scheme of the operation of the optically pumped three-level emitter structure (quantum fountain) based on the asymmetric coupled QWs design. The three levels of the optically pumped emitter corresponding to three electron subbands in the well are indicated with different colors. The black straight lines represent the conduction band potential in the Ge/SiGe heterostructure material system. The parabolic dispersion of the electron energy subbands is also depicted (curved dashed lines). The straight arrows represent the radiative transitions, while the curved arrows represent the nonradiative ones.

guarantee radiative emission gain by itself since two crucial conditions must be satisfied: the first is a long nonradiative ISB transition time τ_{20} of the direct energy relaxation channel 2 → 0, so as to build up a large population of the upper laser level during the pump pulse and to increase the duration of the lasing after the end of the pump pulse (only pulsed operation of the emitter is targeted throughout this work); the second is that the ISB transition time τ_{10} of the 1 → 0 relaxation has to be shorter than the transition time τ_{21} of the 2 → 1 relaxation so as to ensure, after pumping, population inversion between levels 2 and 1 (i.e., $n_2 - n_1 > 0$ where we indicate by n_i the electron density in level i, which is directly proportional to the laser gain. In fact, the population inversion can be approximately related to the ISB relaxation times through the relationship $(n_2 - n_1) \sim (1 - \tau_{10}/\tau_{21})n_2$.[37] The upper laser state population n_2 decreases after pumping mostly due to the interaction between electrons and phonons (spontaneous emission of photons is much less efficient than the nonradiative decay by phonon emission). Finally, achieving actual lasing also depends on the balance between emission gain and losses which, in the case of doped QWs in the far-infrared range with thick active regions, are dominated by free carrier absorption due to polarization leakage.[38,39] Note that charge conservation implies that the total 2D charge density in the QW satisfies $n_{2D} = n_0 + n_1 + n_2$.

In the present work, we developed band-engineered germanium QW heterostructures epitaxially grown on silicon wafers,[40] and we employed novel far-infrared pump−probe measurement setups with the goal of quantitatively determining the relevant physical parameters that may lead to population inversion and positive gain under pulsed optical pumping. We have designed, grown, and characterized by infrared spectroscopy a number of "quantum fountain" samples based on the electron-doped Ge/$Si_{1-x}Ge_x$ heterostructure material.[12,15,41] We have then used narrowband picosecond pulses from a tunable far-infrared free electron laser (FEL) to pump electrons from level 0 selectively into level 1 or 2.[11−14,42−44] Using short broadband (Fourier-transform limited) terahertz time-domain spectroscopy (THz-TDS) pulses to probe the ISB dynamics,[45] we have experimentally determined the global electron energy relaxation time τ_R in which the electron distribution in all subbands relaxes after pumping to the equilibrium Fermi distribution at the base lattice temperature. We have identified the relationship of τ_R to the different ISB relaxation times τ_{kj} ($0 \le j < k \le 2$), calculated with an out-of-equilibrium model of the ISB population dynamics. By spectroscopic analysis of the transmitted probe pulses, we have also determined the free carrier losses as a function of optical pump intensity P. Extrapolating the gain coefficient to values of P higher than those used in the present work, we obtain clear indications that terahertz emission can be achieved (e.g., by electromagnetic cavity design)[46] in the present active material structures grown on silicon wafers.

Our strategy was to leverage on the relatively long ISB relaxation times observed in group-IV materials[44] due to the nonpolar character of the electron−phonon interaction[47] to design QW structures that may fulfill the conditions for lasing. We have implemented one of the possible "quantum fountain" designs based on two asymmetric coupled quantum wells (ACQW).[37] Therein, a thin potential barrier for electrons is realized between two QWs of different width which would feature different energies of the quantized states if isolated from each other. The barrier, obtained by growing few atomic layers of $Si_{1-x}Ge_x$ between the Ge wells, is so thin that the electron wave functions are delocalized in the two wells. One not only does obtain three ISB transitions at energies E_{02}, E_{12}, and E_{01} selected by design[48] but also can tune the transition matrix elements among the levels by designing the corresponding spatial overlap of the electron wave functions.[13] Another important mechanism that we exploit for engineering the transition times is to set the laser transition energy E_{12} below the energy thresholds for optical phonon emission.[11] This condition sets the emission frequency range of our devices in the far-infrared below 6 THz, which still leaves plenty of bandwidth for applications like intrachip wireless data transfer or on-chip chemical sensing. Because of the high sensitivity of the quantum design to both geometry and material parameters, an experimental verification by steady-state and pump−probe terahertz spectroscopy is necessary, and this is the subject of the present work.

METHODS

The quantum state design of our samples was performed employing a multivalley self-consistent effective mass calculation,[49] in order to obtain the proper conduction band profile at the L-point of the reciprocal space, the energies of the levels

DOI: 10.1021/acsphotonics.5b00561
ACS Photonics 2016, 3, 403−414

confined in the asymmetric structure and the corresponding wave functions (see Figure 2).[15] We verified that the Δ_2-valley minima in the barriers are higher in energy than level 2, so their presence can be neglected (see Supporting Infromation). We have varied the heterostructure parameters within the experimentally available ranges determined in our previous works.[50−52] In germanium, there exist two main nonpolar optical phonon branches that provide fast, although non-resonant, energy relaxation channels to electrons in the excited states:[10] the zone-center phonon at $E_{ph,\Gamma}$ = 37 meV, which features negligible momentum transfer to the electrons that therefore remain in the same valley (intravalley phonon relaxation), and the [111] zone-boundary phonon at $E_{ph,\Lambda}$ = 25 meV that connects electronic states in two different valleys among the four equivalent valleys centered at the L-point of the Fermi surface of electron-doped germanium (intervalley phonon relaxation). Without entering all the details of the electron−phonon interaction,[53−55] here we just recall that $E_{ph,\Lambda}$ and $E_{ph,\Gamma}$ set the two main energy thresholds for optical phonon emission by electrons: because of energy conservation, the nonradiative ISB transitions with energy smaller than $E_{ph,\Lambda}$ are driven by the much slower emission of acoustic phonons.[11] Therefore, the design choice we made for having a long τ_{21} was to require $E_{12} < E_{ph,\Lambda}$ so that no optical phonon can be emitted in the 2 → 1 nonradiative relaxation. This condition sets the emission frequency in the range below 6 THz (photon energies <25 meV). However, on the basis of the same energy conservation mechanism, a short τ_{10} was obtained under the condition $E_{01} \sim E_{ph,\Lambda}$. $E_{02} = E_{01} + E_{12}$ had to be larger than all energy thresholds for phonon emission, and therefore, we resorted to wave function overlap design to obtain a τ_{20} as long as possible. In Figure 2, one sees the predicted squared modulus of the wave functions $\psi_0(z)$, $\psi_1(z)$, and $\psi_2(z)$ of the first three levels confined in the conduction band of a typical ACQW structure. Symmetry breaking activates the 0 → 2 transition dipole in the wide well, which is needed for optical pumping. As said above, the barrier thickness is the fine-tuning material-growth parameter for determining the relaxation time ratio τ_{10}/τ_{21}, as it sets the penetration of $\psi_2(z)$ into the wide well and thus its overlap with $\psi_0(z)$ and $\psi_1(z)$. An upper value to τ_{21} is set by acoustic phonon emission through the deformation potential scattering,[54,55] an effect that we do not consider here explicitly, but it is known to provide an approximate time scale above 200 ps for ISB relaxation in germanium quantum wells.[11,56] We will therefore employ the upper limit value of 200 ps for all transition times when they are found to exceed this value in the out-of-equilibrium model. The third excited state $\psi_3(z)$ is much higher in energy, and it does not participate to the quantum fountain emission process.

The sample growth was conducted in an ultrahigh vacuum chemical vapor deposition (UHV-CVD) reactor, where the Ge/SiGe QW system is epitaxially grown on top of a Si(100) wafer. In order to populate the fundamental level, n-type doping of the wide Ge well was achieved through phosphine (PH_3) codeposition in the wide well region.[40,41] The barrier composition was $Si_{0.18}Ge_{0.82}$, which we determined to be the highest possible Si content in our growth chamber to achieve reproducible band offset values for reliable quantum design.[15] The structural characteristics and the predicted transition energies are shown in Table 1. In order to increase the optical absorption path length, the ACQW structure was repeated 20 times, separated by 30 nm-thick undoped spacers, for a total thickness of the QW stack of ∼1 μm.

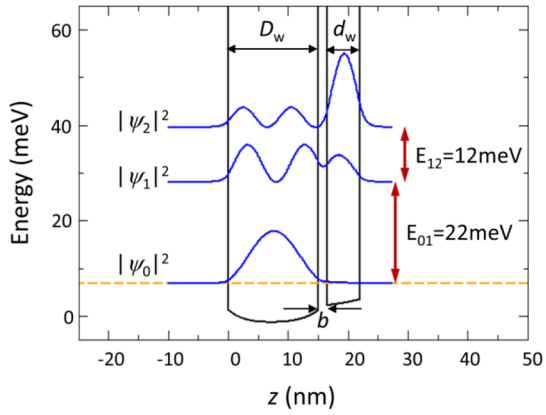

Figure 2. Band-structure model results for conduction band profile at L-point (black line) and squared modulus of level wave functions (blue lines) confined in the structure featuring a wide well of width D_w = 15 nm and a narrow well of width d_w = 5.5 nm, separated by a barrier of thickness b = 1.5 nm. The yellow dashed line represents the calculated Fermi level position. The predicted ISB transition energies (red arrows) are also displayed.

Table 1. Structure Parameters for the Three Investigated Samples: Wide Well Width D_w, Narrow Well Width d_w, Central Barrier Thickness b, and Calculated ISB Transition Energies E_{01}, E_{02}, and E_{12}

sample	D_w (nm)	d_w (nm)	b (nm)	E_{01} (meV)	E_{02} (meV)	E_{12} (meV)
1955	15	3.5	1.5	23	48	25
1953	15	5.5	1.5	22	34	12
1949	13	4.5	1.5	26	41	15

The steady-state ISB absorption spectra have been measured in side-illuminated multipass waveguide configuration with a Fourier-transform infrared (FT-IR) spectrometer equipped with a helium-flow cryostat, a wire-grid polarizer, and a liquid-helium bolometer. We used a single-metal waveguide configuration in which the face of the silicon wafer where the QWs are grown is coated with a metal bilayer (Ti/Au, 10 nm/100 nm) while the opposite face works as the second interface, confining the radiation via total internal reflection.[14,43] To this aim, the input facet of the waveguide was polished at an angle of 45° relative to the QW growth plane, and the wafer thickness was selected to be 0.8 mm to increase the waveguide aperture. In this configuration, the radiation electric field propagating through the QW layers is TM-polarized, i.e., orthogonal to the growth plane and almost parallel to the ISB transition dipole.[3] When the input radiation is TE-polarized, the ISB transitions are not probed because the field intensity of the TE mode is zero at the metal−semiconductor interface. The reference spectra for TM and TE polarizations were measured through an empty slit of the same dimensions of the transverse waveguide section (5.0 × 0.8 mm^2) and used to obtain the corresponding absolute waveguide transmittances $S_{TM}(\omega)$ and $S_{TE}(\omega)$ as a function of the electromagnetic frequency ω. The range of the FT-IR measurements is limited at low photon energies to 15 meV. In order to extend the measurement range, in one case (sample 1953) we used THz-TDS with GaP electro-optic crystals that display broader emission range but lower electro-optic coefficient if compared to those of ZnTe.[57,58]

The system relaxation dynamics back to the equilibrium after optical pulsed excitation has been studied in the framework of

DOI: 10.1021/acsphotonics.5b00561
ACS Photonics 2016, 3, 403−414

an out-of-equilibrium model in which the delay-time dependent electron temperatures $T_{e,0}$, $T_{e,1}$, and $T_{e,2}$ in the three subbands are separately defined, and the entire electron system is allowed to relax energy toward the lattice, considered as a thermal bath at a base temperature T.[47,59] We assume that the electron population in each subband thermalizes at a fast time scale, therefore three delay-time dependent electron temperatures and quasi-Fermi levels have been introduced for the three subbands. Their dynamical evolution has been self-consistently calculated from the energy and particle flux occurring among the three subbands at each time step, which in turn are determined by the electron temperatures and quasi-Fermi levels at the previous time step. The only allowed energy relaxation channel is the electron-optical phonon interaction, in both inter and intrasubband relaxation processes, considering the two relevant optical phonon bands (Λ and Γ, see above). The model is used to calculate the individual subband populations after absorption of the pump pulse and their evolution as a function of pump−probe delay t'. The differential transmittance change relative to pump-off conditions $\Delta S/S(t') = (S(t') - S_{off})/S_{off}$ is also determined numerically at various ω from the electron population and total kinetic energy calculated for each subband. It is found that, when pumping above the 0 → 2 ISB transition at different values of P and T, a single energy relaxation time scale (a "calculated" τ_R) approximately governs both $\Delta S/S(t')$ and the population change of the three subbands $\Delta n_i/n_{2D} = (n_i(t') - n_{i,off})/n_{2D}$ in the range 10−400 ps. When pumping at the 0 → 1 ISB transition, more complicated dynamics with multiexponential behavior is obtained in the model; therefore, a broad range of τ_R values is identified. The quantity $\Delta S/S(t')$ and the calculated τ_R can be directly compared to the experimental pump−probe data and the experimental τ_R.

The relaxation dynamics at different P and T have been measured with a picosecond narrowband THz-pump broadband THz-probe setup (shown in Figure 3). The far-infrared FEL FELBE is employed for tunable narrowband pumping. The FEL emits pulses with a repetition rate of 13 MHz (77 ns pulse-to-pulse separation) and pulse length around 10 ps. The emission wavelength can be tuned in the far-infrared range by changing the undulator gap of the FEL cavity.[60] We selected a wavelength of 50 μm (photon energy of 25 meV) for pumping the 0 → 1 transition and a wavelength of 30 μm (photon energy of 41 meV) for pumping the 0 → 2 transition. The waveguide samples were mounted on the cryostat in such a way that both the pump and the probe radiation propagate through the samples in a TM-configuration, in order to pump and probe the ISB transitions. In our experiment, the pulse energy at the exit of the FEL beamline was adjusted with a set of attenuators in the 3 to 30 nJ range, corresponding to a pump power density at focus inside the sample from 8 to 80 kW/cm^2, taking into consideration reflection and absorption losses in all inserted optical elements (Figure 3). For each FEL wavelength, we have applied pump powers high enough to excite about 5% (0.5%) of the ground-state electrons into the first (second) excited state[56] avoiding steady-state sample heating. To study the relaxation back to equilibrium in different conditions, the sample was cooled down to T = 37 K and T = 97 K with a liquid helium cryostat. For probing, a THz-TDS was employed. Here, the probe beam was a quasi-single cycle THz pulse generated by optical rectification in a ZnTe electro-optic crystal excited by a near-infrared ultrafast pulse of a Ti:sapphire (Ti:Sa) regenerative amplifier (center wavelength 800 nm, pulse width 40 fs, and repetition rate 250 kHz) synchronized with the FEL pulses. The detection is performed with a second ZnTe rectifying crystal (ZnTe (2) in Figure 3) and subsequent polarization-resolving detector connected to a lock-in amplifier (not shown in the Figure). The bandwidth of the rectified pulse extends from about 0.1 THz up to 2.9 THz (photon energy range 0.4 to 11.5 meV). Detection at higher frequencies is prevented by phase-matching conditions due to ZnTe crystal thickness. However, diffraction effects in our waveguide sample impose a low-frequency spectral cutoff around 0.7 THz, where the free-space wavelength is 400 μm or half the waveguide thickness.

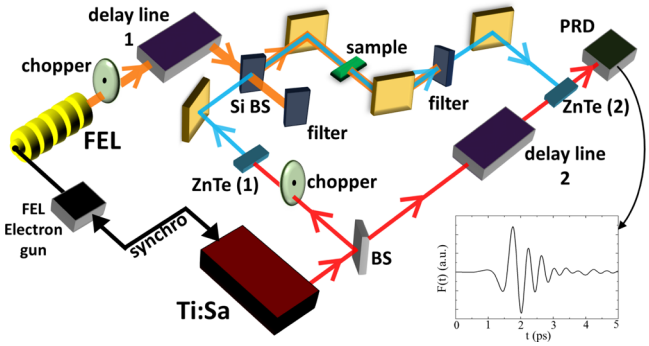

Figure 3. Scheme of the pump−probe setup: the free electron laser (FEL), generating the pulsed pump beam, and a Ti:Sa regenerative amplifier are synchronized electronically. ZnTe electro-optic crystals are used for THz probe pulse generation (ZnTe (1)) and detection (ZnTe (2)) with a glass beam splitter (BS, light gray) directing two portions of the Ti:Sa beam toward the two ZnTe crystals. Delay line 1 is used for delay-time-resolved pump−probe measurements, while delay line 2 is used for THz-field time-trace acquisitions. Optical choppers enable lock-in detection of the polarization-resolving diode pair (PRD) signal. Four parabolic mirrors (yellow squares) collect and refocus the pump and the probe beams on the sample. The silicon beam splitter (Si BS) combines the FEL pump and the THz-TDS probe pulse collinearly, while the low-pass filters block the FEL beam but not the THz-TDS probe beam. The FEL beam is indicated in orange, the Ti:Sa beam in red, and the THz probe beam in light blue. The inset shows an example of the acquired THz-field time-trace.

The pump−probe setup in Figure 3 features two delay lines for two different types of acquisition: scanning the "delay line 1" in Figure 3 allows one to obtain the transmitted THz intensity as a function of probe−pump delay t' with a long scan range ($-50 < t' < 400$ ps). However, scans with the "delay line 2" in Figure 3 producing time-domain THz-field traces as a function of time $F(t)$ are acquired for a given pump−probe delay or in the absence of optical pump. The first kind of acquisition is used for evaluation of the relaxation times. The $F(t)$ traces obtained in the second kind of acquisition are Fourier-transformed into transmitted intensity spectra $H(\omega)$ for the discrimination of free carrier losses and optical transition bleaching effects. The relative transmitted intensity change curves are obtained by subtracting $H_{off}(\omega)$, measured before the pump pulse arrives on the sample, from $H_{on}(\omega)$, measured at pump−probe time coincidence. Before performing the Fourier transformation, the $F(t)$ traces are cut after 10 ps from the leading edge, a value corresponding to the pump pulse duration that still enables a sufficient spectral resolution of 0.1 THz.

In order to interpret the spectrally resolved data, we used an electrodynamic model for radiation transmission through a thin film taken from ref 61. Following this model, the transmittance

DOI: 10.1021/acsphotonics.5b00561
ACS Photonics 2016, 3, 403−414

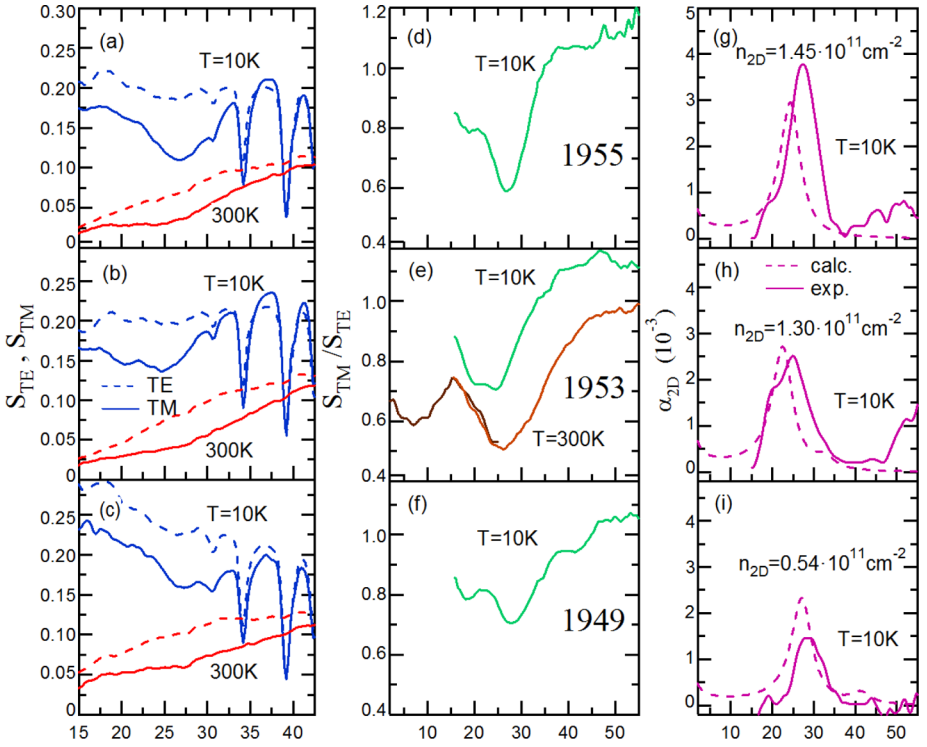

Figure 4. (a–c) TM (solid) and TE (dashed) FT-IR transmission spectra for samples 1955 (a), 1953 (b), and 1949 (c) acquired at low-T (blue) and room-T (red). (d–f) Dichroic transmission ratio at low-T (green) for the three samples; for sample 1953, it is also reported at room-T (brown) extended to lower frequencies using a THz-TDS apparatus with GaP electro-optic crystals (dark brown). The dip at 18 meV in (d–f) is an artifact due to the transmission function of the polarizer. (g–i) Calculated (dashed) and experimental (solid) 2D absorption coefficient, the latter obtained from the baseline-corrected data of panels (d–f), respectively.

of a thin absorbing film on a transparent substrate of refractive index η can be written in terms of the complex conductivity of the film as

$$S(\omega) = \frac{4\eta}{(Z_0 d\sigma' + \eta + 1)^2 + (Z_0 d\sigma'')^2} \quad (1)$$

where $\tilde{\sigma}(\omega) = \sigma'(\omega) + i\sigma''(\omega)$ is the complex optical conductivity of the film. The absorption path length d and the refractive index η were set to $d = 14$ μm and $\eta = 3.5$, while $Z_0 = 377$ Ω is the free space impedance. The value of d accounts for an optical path of $2/\cos(45°)$ times the QW stack thickness of 1 μm for each reflection, times 5 reflections along the waveguide length. The optical conductivity in the TM polarization is modeled as the sum of three Lorentz oscillators representing the three ISB transitions from level j to level k ($0 \le j < k \le 2$). Additionally, we include a Drude term representing free carrier response excited by the field component parallel to the QW plane, which increases above zero with increasing distance from the metal. Indeed, only the QWs close to the metal are probed in a pure TM polarization. Electromagnetic simulations suggest a value $A = 0.04$ for the polarization leakage factor that multiplies the Drude term. We thus write

$$\tilde{\sigma}(\omega) = \frac{A\cdot\sigma_D}{1 - i\omega/\gamma_D} + \sum_{j<k} \frac{\omega I_{L,jk}}{i(\omega_{L,jk}^2 - \omega^2) + \omega\gamma_{L,jk}} \quad (2)$$

where σ_D is the Drude conductivity, γ_D is the Drude scattering rate, while $\omega_{L,jk}$, $\gamma_{L,jk}$, and $I_{L,jk}$ are the Lorentz oscillator frequency, line width and strength, respectively. $\gamma_{L,jk}$ is set by the ISB transition line width, the Lorentz oscillator frequencies are set by the relationship $\hbar\omega_{L,jk} = E_{jk}$, and the Lorentz oscillator strength $I_{L,jk} \propto (n_j - n_k)$ can become negative in case of population inversion between levels j and k. The quantity $\sigma_D\gamma_D$ is called the Drude weight, and it is proportional to the energy dissipated by free carriers. At equilibrium only, it can be demonstrated through the optical sum rules that the Drude weight is proportional to the three-dimensional carrier density $N_{3D} = n_{2D}\cdot d_w$.[62] Out of equilibrium (e.g., after pumping), the Drude weight can be higher than its equilibrium value because the electron distribution is different from the Fermi–Dirac equilibrium distribution. Best-fit values for all Drude–Lorentz parameters were found by fitting eq 1 to the steady-state transmittance spectra displayed in Figure 4. The relative pump-induced spectral change of the transmitted intensity of the THz-TDS pulse $\Delta H/H = [H_{on}(\omega) - H_{off}(\omega)]/H_{off}(\omega)$ is equal to the absolute transmittance change at pump–probe coincidence $\Delta S/S(0)$ at each ω. We have thus modeled the spectrally resolved pump–probe data $\Delta H/H$ measured for different P when pumping the $0 \rightarrow 2$ transition by allowing $I_{L,jk}$ and σ_D in $\tilde{\sigma}(\omega)$ to vary as a function of P. Only the variation of the Drude weight and Lorentz oscillator strengths under pumping are left as free parameters to fit the model curves to the measured $\Delta H/H$ spectra in Figure 6, and the spectra are reasonably reproduced given the small number of degrees of freedom.

The laser gain spectra $G(\omega)$ for different P plotted in Figure 7 were obtained from the electrodynamic model of the spectrally resolved pump–probe data in Figure 6 described above. The global absorption coefficient $\alpha(\omega) = -G(\omega)$ can be derived from $\tilde{\sigma}(\omega)$ by standard electrodynamics relationships,[62] and the gain can become positive only if population inversion

DOI: 10.1021/acsphotonics.5b00561
ACS Photonics 2016, 3, 403–414

occurs in levels 1 and 2, i.e., $I_{L,12} \propto (n_1 - n_2) < 0$. From a fit to the data in Figure 6, we determined the (positive) change in the absorption coefficient of free carriers and the (negative) change in the ISB absorption strength under pumping at given P. Looking at the resulting fitting parameters in Table 3, the free carrier absorption increase is assumed to saturate with increasing P exponentially around $P \sim 300$ kW/cm^2, while the 1 → 2 ISB bleaching strength is assumed to increase linearly with P at least up to 1 MW/cm^2, a value of P at which the fraction of electrons brought to level 2 by the pump is still negligible when compared to the total electron density at level 0. The different behavior with increasing P of pump-induced free carrier losses and upper level population is in agreement with previous works[33,63] and previous observations in one-color pump−probe experiments performed with the same FEL source up to $P \sim 250$ kW/cm^2 on single Ge/SiGe QWs.[56] We therefore extrapolated the trend of the model parameters to high P (up to 1 MW/cm^2), and we calculated the projected gain spectra of Figure 7.

RESULTS

In Figure 4a−c, we display the waveguide transmittances $S_{TM}(\omega)$ and $S_{TE}(\omega)$ measured by FT-IR as a function of the photon energy $E = \hbar\omega$. The ISB transitions appear as broad dips only in the TM transmission spectra where the radiation electric field is nonzero in the QW stack.[3,51] In Figure 4a−c, the dips appear more clearly in the low-T (T = 10 K) spectra but also in the room-T (T = 300 K) ones. The narrow absorption lines at 34 and 38 meV, instead, are due to hydrogenoid trapped carriers in the lightly doped silicon substrate, and therefore, they appear in both TM and TE transmittances only at low T. In general, the ISB transitions are more clearly detected in Figure 4d−f showing the dichroic transmission spectra S_{TM}/S_{TE} (i.e., the ratio between the two spectra obtained in the different polarizations TM and TE), in which all polarization-independent features compensate (including the narrow lines due to hydrogenoid carriers). At T = 10 K, only the 0 → 1 transition is observed, centered between 22 and 26 meV for different samples (see Table 1). The dipole selection rule inhibiting the 0 → 2 transition is violated due to asymmetry of the QW structure, but, by design, the wave function overlap between level 0 and 2 is very low in our structures, leading to a small absorption cross-section at E_{02}. Moreover, level 1 is empty at T = 10 K and the 1 → 2 transition cannot be observed, although allowed by the selection rule. At room-T, the 1 → 2 transition should be observed due to the significant thermal population of level 1; however, depending on the sample, it falls either out of the range of the FT-IR setup or within the broad range of the more intense dip related to the 0 → 1 transition. Panels g−i display the 2D absorption coefficient $\alpha_{2D}(\omega)$ in the range of the 0 → 1 transition obtained both from the low-T spectra of panels d−f, respectively, by dividing for a baseline[3,51] (purple continuous lines) and from the transition matrix element caclulation assuming $N_{3D} = 1{\cdot}10^{17}$ cm^{-3} (purple dashed lines). Frequency integration of the experimental spectra in Figure 4g−i provides the values of the activated carrier density n_{2D} reported in the panels for the three samples. The calculation $N_{3D} = n_{2D}{\cdot}d_w$ provides the experimental values $0.96{\cdot}10^{17}$, $0.87{\cdot}10^{17}$, and $0.41{\cdot}10^{17}$ cm^{-3} for samples 1955, 1953, and 1949, respectively. The slight disagreement between calculated and measured ISB transition energies can be due to both thickness uncertainty governed by interface roughness (which is of the order of 0.4 nm; see Supporting Information) and uncertainty in the charge density in the well that ultimately sets the transition resonance after consideration of the depolarization shift.[52,56]

The general increase of the transmittance with cooling is due to recapture of free carriers in the silicon substrate by dopant atoms, a fact that strongly reduces absorption losses in the silicon substrate. The free carriers in the QWs remain confined in the z direction, but they are highly mobile in the x−y plane at all T. Moreover, they display nonzero absorption in the TM polarization (see Methods) and therefore constitute a loss mechanism that competes with laser gain. Starting from Figure 4a, we see that sample 1955 displays an intense ISB absorption (approximately 40% maximum attenuation) centered at 26 meV, compatible with the calculated value of 23 meV, and full width at half-maximum of 4.4 meV that compares well with that found in previous works.[50,51] The much weaker 1 → 2 transition falls at E_{12} = 25 meV, well inside the 0 → 1 transition dip, and it is therefore not observable even at room-T. In Figure 4b, the transmission spectra of sample 1953 are shown. The wide well thickness is 15 nm as for sample 1955; hence, the 0 → 1 transition appears almost at the same energy (E_{01} = 25 meV). The larger thickness of the narrow well (5.5 nm compared to 3.5 nm in sample 1955) sets the predicted 1 → 2 transition energy to E_{12} = 12 meV. This value is outside the range of our FT-IR setup in waveguide configuration, but it is accessible to THz-TDS performed using GaP electro-optic crystals. Figure 4e depicts the spectra obtained by merging the FT-IR dichroic spectra S_{TM}/S_{TE} and the same quantity measured at room-T by THz-TDS, rotating the sample in the THz-TDS beam to acquire the transmittance in TE-polarization. In the room-T merged dichroic spectrum, the 1 → 2 transition appears as a broad dip centered around 10 meV, less intense than the 0 → 1 transition. The photon energy of E_{12} = 10 meV corresponds to an electromagnetic frequency of 2.4 THz that falls in the range provided by broadband THz-probe pulses of our THz-TDS setup, thus allowing us to measure the 1 → 2 transition bleaching in this sample with increasing P (see below). Finally, in sample 1949 (Figure 4c), the narrow well thickness was reduced to 4.5 nm when compared to that of sample 1953, and the wide well thickness was reduced to 13 nm. Correspondingly, the 0 → 1 transition appears at slightly higher energy E_{01} = 28 meV. The 1 → 2 transition is predicted at E_{12} = 15 meV but is not clearly observed in our FT-IR spectra at room-T possibly due to the lower N_{3D} obtained in this specific sample. In general, the steady-state spectra confirm that the asymmetric Ge/SiGe QW structures display clear ISB features and provide quantitative information for the models and the analysis of the pump−probe data.

We now turn to the determination of the picosecond relaxation dynamics of the three levels under optical pumping in the presence of the asymmetric coupling between the two wells. We generate nonequilibrium populations of the three levels by optical pumping with FEL pulses. We keep the "delay line 2" position (see Figure 3 and Methods) fixed at time t where $F(t)$ reaches its absolute maximum peak value $F_{max,0}$, i.e., close to the leading edge of the THz-TDS pulse. The relaxation dynamics after pumping are then monitored by measuring, as a function of the pump−probe delay time t' (delay line 1 in Figure 3), the return of $F_{max}(t')$ to its equilibrium value $F_{max,0}$ that it displayed before the pump pulse arrived. Physically, $\Delta F_{max}(t') = F_{max}(t') - F_{max,0}$ is distinct from the optical transmission at the pumped ISB transition frequency, and it is instead determined by the transmitted intensity change

DOI: 10.1021/acsphotonics.5b00561
ACS Photonics 2016, 3, 403−414

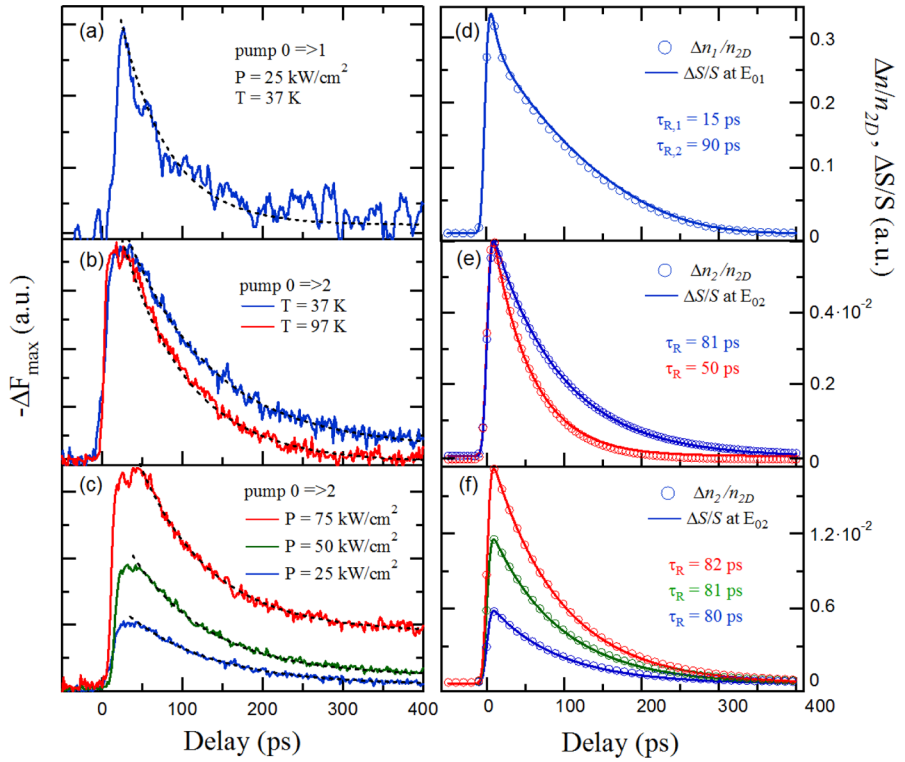

Figure 5. Relaxation dynamics of sample 1953. Left column: data (continuous lines) and fits (black dashed lines) of the THz electric field intensity change as a function of pump−probe delay for different temperatures T and pump intensities P. Right column: results of the out-of-equilibrium model for the optical transmittance change $\Delta S/S$ and the variation in the population of the pumped level referred to the total electron density $\Delta n/n_{2D}$ at the corresponding P and T values. (a,d) Pump photon energy of 25 meV; (b,e) pump photon energy of 41 meV at different Ts (blue 37 K, red 97 K); (c,f) sample pump photon energy of 41 meV at different pump intensities: 25 kW/cm^2 (blue), 50 kW/cm^2 (green), and 75 kW/cm^2 (red). The right scale values refer to either $\Delta n_1/n_{2D}$ (panel d) or $\Delta n_2/n_{2D}$ (panels e,f). $\Delta n_2/n_{2D}$ is much lower than $\Delta n_1/n_{2D}$ because of much lower absorption strength of the $0 \rightarrow 2$ transition if compared to the $0 \rightarrow 1$ transition.

Table 2. Experimental (Sample 1953) and Calculated Relaxation Times τ_R for Optical Phonon Scattering at Different Pump Photon Energies E_{FEL}, Pump Intensities P, and Temperatures T, and the ISB Relaxation Times τ_{kj} Directly Obtained from the out-of-Equilibrium Model[a]

T (K)	P (kW/cm^2)	E_{FEL} (meV)	τ_R (exp) (ps)	τ_R (calc) (ps)	τ_{10}(calc) (ps)	τ_{20}(calc) (ps)	τ_{21}(calc) (ps)
37	17	25	60	15−90	15−90		
37	25	41	106	80	30	100	$>\tau_{AC}$
37	50	41	96	81	30	90	$>\tau_{AC}$
37	75	41	88	82	30	90	$>\tau_{AC}$
97	60	41	81	50	6	90	200

[a]In the case of τ_{21} at 37 K, the obtained values are larger by one order of magnitude than the acoustic phonon relaxation $\tau_{AC} \sim 200$ ps. Other non-phonon mediated scattering mechanisms also contribute to set an upper limit for the relevance of optical phonon scattering in the electron energy relaxation.

spectrally integrated between 0.7 and 2.9 THz. In this frequency range, free carrier absorption dominates the response. Free-carrier absorption increases when the pump pulse arrives and then returns to its equilibrium value. Assuming a single-exponential behavior, it is possible to effectively extract experimental values for τ_R by fitting the data to the following equation:

$$\Delta F_{max}(t') = \Delta F_{max}(0) e^{-t'/\tau_R}$$

where $\Delta F_{max}(0)$ is the electric field change at pump−probe coincidence ($t' = 0$) relative to its equilibrium value $F_{max,0}$. The quantity $\Delta F_{max}(t')$ was found to be negative in all cases, as expected in free-carrier absorption increase; therefore, it is reported as $-\Delta F_{max}(t')$ in Figure 5a−c for clarity. The negative sign of the spectrally integrated quantity $\Delta F_{max}(t')$ does not exclude that the THz transmittance may increase under pumping at specific THz frequencies, e.g., at the energy of the $1 \rightarrow 2$ ISB transition. Spectral analysis of the entire TDS time trace $F(t)$ taken at both $t' = 0$ and $t' < 0$ is needed to discriminate transition bleaching effects, as described in the next paragraph. The extracted τ_R for sample 1953 are reported in Table 2. For each optical pump level, in Table 2 the calculated value of τ_R obtained by fitting the numerically calculated $\Delta S/S(t')$ curves, displayed in Figure 5d−f, is also reported. Panel d (e,f), also shows the population of level 1 (level 2) which displays almost the same relaxation time scale as $\Delta S/S(t')$. Finally, in Table 2 the ISB relaxation times directly obtained from the out-of-equilibrium model are also reported: it is clear that, in a three-level system, the ISB transition rate to the ground state alone cannot explain the population dynamics

DOI: 10.1021/acsphotonics.5b00561
ACS Photonics 2016, 3, 403−414

of the corresponding excited level, and it is necessary to simultaneously consider the interplay of electrons in the three levels with the lattice in the framework of an out-of-equilibrium model of the ISB dynamics.

The interpretation of the time-resolved data of Figure 5 is as follows. When pumping at $E_{FEL} = E_{01} = 25$ meV ($\lambda_{FEL} = 50$ μm), due to the large absorption coefficient of the 0 → 1 transition, large population variations are generated (variation of $T_{e,1}$ of ∼20 degrees). One could expect that the energy relaxation after pumping at E_{01} is dominated by 1 → 0 transitions by phonon emission because $n_2 \sim 0$. By inspecting the phonon spectrum of Ge, we see that in our samples E_{01} is smaller than $E_{ph,\Gamma} = 37$ meV, while it roughly matches the value of $E_{ph,\Lambda} \sim 25$ meV; therefore, the direct 1 → 0 relaxation takes place by intervalley optical phonon emission with large momentum and energy $E_{ph,\Lambda}$, which is a rather slow process when compared with intravalley emission of phonons with zero momentum and energy $E_{ph,\Gamma}$. This fact is confirmed by the long relaxation times of 30 to 60 ps found in one-color pump−probe experiments on two-level symmetric Ge QW samples with $E_{01} = 25$ meV and interpreted as direct 1 → 0 relaxation by optical phonon emission.[44,47] In apparent agreement with such observations, the present experiment (Figure 5a) provides, for identical E_{FEL} and E_{01}, an approximate relaxation time scale $\tau_{R,exp} \sim 60$ ps. However, the out-of-equilibrium model (Figure 5d) yields a double-exponential relaxation with $\tau_{R,calc1} \sim 15$ ps and $\tau_{R,calc2} \sim 90$ ps. This peculiar behavior has been identified in the model with a competing energy relaxation channel that involves level 2. In this competing channel, a first "inverted" 1 → 2 energy relaxation process takes place by transitions of hot electrons in the subband 1 into the bottom of subband 2. The second slower energy relaxation process is driven by 1 → 0 and 2 → 0 transitions with emission of phonons, and all electron temperatures slowly tend to their equilibrium value. We conclude that this is probably the correct interpretation of the experiment when pumping at $E_{FEL} = E_{01} = 25$ meV shown in Figure 5a, where the signal-to-noise ratio does not allow one to distinguish between single- and double-exponential decays. The trivial analogy with two-level symmetric Ge QW samples with the same value of E_{01} is instead to be rejected, indicating the key role played by subband 2 in energy relaxation processes.

When pumping at $E_{FEL} = 41$ meV ($\lambda_{FEL} = 30$ μm) above the 0 → 2 transition at $E_{02} = 35$ meV (Figure 5 b,c), small population variations are induced due to the small absorption coefficient of the samples (variation of $T_{e,2}$ of few degrees), and a single-exponential fit reasonably reproduces the $\Delta F_{max}(t')$ data with τ_R in the range 80−110 ps (see Figure 5 and Table 2). Fast relaxation by optical phonon emission should be dominant here because $E_{FEL} = 41$ meV > $E_{ph,\Gamma} = 37$ meV. However, due to the small overlap of $\psi_2(z)$ and $\psi_0(z)$ in the ACQW structure (see Figure 2), in the out-of-equilibrium model (Figure 5e,f) we find $\tau_{20} \sim 100$ ps > $\tau_{10} \sim 30$ ps at all T and P levels explored (see Table 2). We can thus safely ascribe the slow relaxation seen after pumping at 41 meV in the experiments to direct 2 → 0 nonradiative transitions by optical phonon emission with $\tau_{20} \sim 100$ ps. The achieved slowing of the 2 → 0 optical phonon emission process is a main achievement of the present work due to wave function engineering. The decrease of τ_R from ∼80 ps at $T = 37$ K to 50 ps at $T = 97$ K (see Table 2) is also consistent with this interpretation. While $\tau_{20} \sim 90$ ps remains almost constant with T because the transition matrix element of the electron−phonon interaction does not depend on T, at higher T a second nonradiative relaxation channel from level 2 to level 1 and then from level 1 to level 0 starts to compete with the direct 2 → 0 channel. This second 2 → 0 energy relaxation channel seems to be activated by absorption of thermally excited phonons.

Quantitative information concerning pump-power thresholds for lasing and gain spectra can be obtained by performing spectrally resolved pump−probe experiments with $E_{FEL} = 41$ meV > E_{02}. We measured the probe transmitted intensity spectra $H_{on}(\omega)$ at pump−probe coincidence ($t' = 0$) and $H_{oFF}(\omega)$ when the probe pulse arrived well before the pump pulse ($t' = -50$ ps). The pump-induced relative transmitted intensity change $\Delta H/H$ (= $\Delta S/S$, see Methods) is shown in Figure 6a, and the corresponding results of the electrodynamic

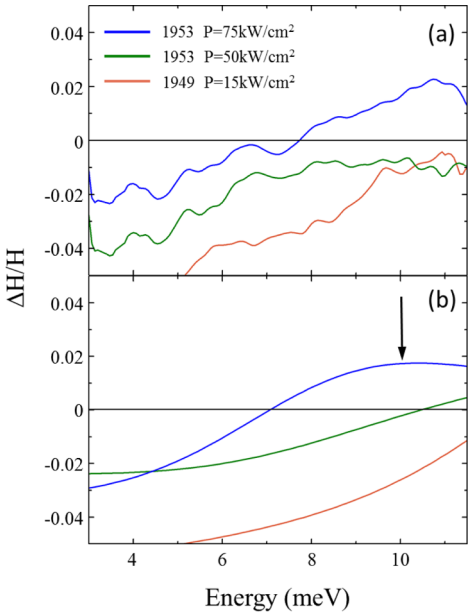

Figure 6. Spectrally resolved data at $T = 37$ K (a) and electrodynamic model (b) of the relative transmitted intensity change of the probe for sample 1953 pumped at 75 kW/cm^2 (blue) and 50 kW/cm^2 (green), and sample 1949 pumped at 15 kW/cm^2 (orange). The arrow at 10 meV indicates the photon energy at which the Lorentzian peak corresponding to the 1 → 2 ISB transition is centered (see text).

model are shown in Figure 6b. The corresponding Drude−Lorentz parameters are reported in Table 3. In sample 1949, one only sees a reduction of $\Delta H/H$ attributed to the increase of

Table 3. Drude−Lorentz Model Parameters from Eq 2 for Two Samples Pumped at Different Pump Intensities P at $T = 37$ K: Drude Conductivity σ_D and Scattering Rate γ_D; Intensity of the Lorentz Oscillator $I_{L,12}$, with Line Width $\gamma_{L,12}$, Centered at Frequency $\omega_{L,12}$ Corresponding to the Nominal 2 → 1 Transition Energy[a]

sample	P (kW/cm^2)	σ_D (Ω^{-1}cm^{-1})	γ_D (cm^{-1})	$I_{L,12}$ (cm^{-2})	$\gamma_{L,12}$ (cm^{-1})	$\hbar\omega_{L,12}$ (meV)
1953	0	40	250	1.12	125	10.4
	50	45	250	1.09	125	10.4
	75	47	250	0.84	125	10.4
1949	0	23	250	0.62	125	15.0
	15	27	250	0.59	125	15.0

[a] γ_D and γ_L are purposely kept constant to a best-fit value for all samples and P.

DOI: 10.1021/acsphotonics.5b00561
ACS Photonics 2016, 3, 403−414

the Drude weight $\sigma_D\gamma_D$. No information can be obtained on the subband populations of sample 1949 because the 1 → 2 ISB transition falls outside the accessible spectral range of the probe in Figure 6. Owing to a smaller electron density in sample 1949, lower P is sufficient to induce relative changes comparable to that of sample 1953 at higher P. In sample 1953, beyond the increase of $\sigma_D\gamma_D$, a reduced strength $I_{L,12}$ of the Lorentz oscillator centered at E_{12} = 10.4 meV is also observed under pumping due to the increased population of level 2 (bleaching), and this explains the positive overshoot of $\Delta H/H$ above 10 meV marked by the arrow in Figure 6. Physically, the increase of $\sigma_D\gamma_D$ under pumping can be explained by the removal of some of the electrons from level 0 that smears the electron distribution over an energy range broader than the equilibrium Fermi distribution function and then reduces the Pauli blocking effect. This corresponds to the negative sign of the measured $\Delta F_{max}(t')$ in Figure 5. Calculating the Fermi−Dirac population factors at T = 37 K for the calculated energy level position at 22 and 34 meV above the Fermi level (which corresponds to the fundamental level; see Figure 2), one finds that 0.08% of the electrons populate level 1 and 50 times less electrons populate level 2. Under these conditions, the 1 → 2 ISB absorption is certainly nonzero, and the optical pumping of electrons from level 0 to level 2 inhibits the 1 → 2 absorption, resulting in the decrease of $I_{L,12}$ under pumping. The small variations of the high-energy oscillator strengths $I_{L,01}$ and $I_{L,02}$ with pumping have no impact on the transmitted intensity in the energy range displayed in Figure 6 and therefore cannot be derived from a fit to the data. For determining the gain in Figure 7, we directly compute them from the calculated n_i.

DISCUSSION

The experimental data in Figures 5 and 6 are well reproduced by the out-of-equilibrium model and by the electrodynamic model, respectively; therefore, we will base the following discussion on both data and models. The main result of the delay-time-resolved pump−probe analysis (Figure 5) is that level 2 is sufficiently long-lived ($\tau_{20} \sim 100$ ps and $\tau_{21} \sim 200$ ps) to achieve, with a short-pulse optical pump, population inversion lasting beyond the pump pulse duration (here 10 ps). A further (expected) result is that the interaction of electrons with nonpolar optical phonons and acoustic phonons determines the nonradiative ISB dynamics, which is rather slow when compared to that of similar structures previously realized on group III−V compound semiconductors.[31,37,46,48] The main result of the spectrally resolved pump−probe analysis (Figure 6) is that, for high enough pump photon density (i.e., peak pump power density), ISB emission gain is expected to surpass the dominant free carrier losses.

The large values for τ_{20} and τ_{21} obtained here in ACQW are compared to the values of few picoseconds obtained in symmetric QWs where the first ISB transition energy was comparable to the present value E_{02} = 35 meV.[56] We ascribe the observed increase of the ISB relaxation time in ACQWs to successful engineering of wave function overlap. In the out-of-equilibrium model, τ_{21} is found to be longer than 1 ns because $E_{12} < E_{ph}$; therefore, it cannot be extracted directly from the experimental data, and we use the typical acoustic phonon scattering time of ∼200 ps[11,56] to calculate $\tau_{10}/\tau_{21} \sim 0.15$. This is an extremely low value,[59] favorable for population inversion between levels 1 and 2, obtained here by exploiting the slow relaxation of the transitions with energy $E_{12} < E_{ph}$,[44] instead of exploiting fast resonant phonon depopulation of level 1 as previously done in quantum fountain devices made of III−V compound semiconductors.[27,29,30]

We now turn to the frequency-resolved data of Figure 6. Pump-induced increase of the free-carrier absorption dominates most of the $\Delta H/H$ spectra, but the 1953 sample pumped at 75 kW/cm^2 (blue curve in Figure 6a) shows a reduction of the oscillator strength of the 1 → 2 ISB transition. From the oscillator strength reduction, we evaluate that 8×10^{14} electrons/cm^3 were brought to level 2 by the pump pulse, leading to a rather low pump-beam absorption in the entire QW region of ∼2%, a value compatible with the low value of the calculated 0 → 2 transition matrix element. This is the main drawback of our ACQW design, which has to be traded with the advantages of long relaxation times and of structure simplicity. The 2D density of electrons per well brought from level 0 to level 2 by the pump pulse at 75 kW/cm^2 is estimated to be $n_2 \sim 2{\cdot}10^7$ cm^{-2}, i.e., 20% of those already present in level 1 ($n_1 \sim 0.0008{\cdot}n_0 \sim 1{\cdot}10^8$ cm^{-2}), meaning that population inversion is not achieved ($n_2/n_1 \sim 0.2 < 1$). In the present experiment, thermal balance issues forced us to limit P to ∼75 kW/cm^2 and T to 37 K. On the basis of the quantitative spectroscopic information presented in this work, we can evaluate the potential for light emission from our QW structure. By increasing P, a larger fraction of electrons can be brought to level 2, and by decreasing T, the population of level 1 rapidly decreases according to the Fermi distribution factor, favoring population inversion even at lower P. Possibly, net spontaneous emission may then take place at lower temperatures,[8] but it could not be probed with the present coherently locked THz-TDS probe that is insensitive to all contributions of the THz field that are not generated in the ZnTe electro-optic crystal emitter. Concerning stimulated emission,[42] which would instead be measurable with the THz-TDS setup, population inversion should be strong enough to overcome the free carrier losses and produce a significant amplification of the THz-TDS probe beam, as we now discuss.

We now turn to the estimate of the gain coefficient for photon energies around E_{12} under pumping above E_{02} due to the balance between emission gain proportional to $(n_2 - n_1)$ and the absorption coefficient $\alpha(\omega)$. Both quantities depend on the optical pumping level P. The latter phenomenon is clearly observed here and in other similar experiments,[47] and it is attributed to pump-induced release of the Pauli blocking for free-electron scattering in the fundamental level, as mentioned above. However, the increase of the Drude oscillator strength for increasing P is found to saturate around 300 kW/cm^2, while the population n_2 of level 2 is predicted to increase linearly with P (see Methods). n_1 can be considered constant with P at pump photon energy E_{02}, and for low enough temperatures (T < 20 K), we can consider $n_1 \sim 0$. Considering this, in Figure 7 we have projected up to P = 1 MW/cm^2 the trends measured here at low P so as to obtain net gain spectra $G(\omega)$ for different P. To do so, we have subtracted both free-carrier and ISB absorption losses (including those centered at E_{02} = 35 meV and E_{01} = 25 meV modeled from the data in Figure 4) from the absolute positive gain curve of intensity proportional to $n_2 - n_1$, assuming a Lorentzian line shape for the gain curve identical to that of the 1 → 2 absorption of Table 3. We have found a threshold pump power density of 500 kW/cm^2 for positive net gain at photon energies between 10 and 25 meV ($2.5 < \omega < 6$ THz). Because of absorption in the silicon substrate, such P levels probably require short-pulsed optical pumping in the picosecond range. A pump power density of 500 kW/cm^2 was

DOI: 10.1021/acsphotonics.5b00561
ACS Photonics 2016, 3, 403−414

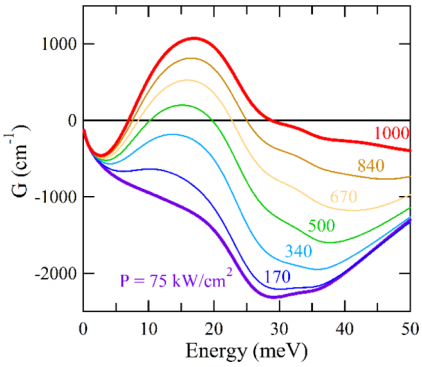

Figure 7. Calculated ISB gain function for increasing pump intensity from the experimental value of 75 kW/cm^2 (violet line) up to 1 MW/cm^2 (red thick line). Positive gain values are predicted for pump intensities above 500 kW/cm^2.

indeed available from the FEL, but it could not be delivered to the sample without significantly increasing its steady-state temperature because of thermal balance limitations. Sample heating is unavoidable in the present waveguide configuration due to pump absorption by the 800 μm thick silicon substrate[64] and by the free-carriers in the QWs due to polarization mixing. Both types of losses could be suppressed by electromagnetic engineering of the laser cavity, e.g., by the use of double-metal waveguides that would make the electromagnetic mode purely TM.[65] Future works will focus on designing suitable optical pumping schemes for obtaining lasing action from Ge/SiGe QWs on silicon substrates based on the quantitative information here reported.

In conclusion, we have presented the design and the first steps of experimental characterization of a terahertz emitter on silicon substrate based on three-level Ge/SiGe asymmetric coupled quantum wells, also called the quantum fountain structure. Our spectrally resolved terahertz picosecond pump−probe measurements have displayed transmission increase above 2.5 THz related to bleaching of the transition between the two upper levels 2 and 1. Such an important result was achieved by quantum-engineered symmetry breaking in the ACQW structure that enables optical pumping of electrons from level 0 to level 2 preventing fast reverse relaxation. The pump−probe delay-time-resolved data, interpreted through an out-of-equilibrium model of the intersubband dynamics, have shown that the 1 → 0 transition rate is higher than both the 2 → 0 and 2 → 1 rates as expected from the quantum fountain structure design. We obtain an intersubband transition time ratio $\tau_{10}/\tau_{21} \sim 0.15$ favorable for strong population inversion between level 2 and level 1. Moreover, the rather long lifetime of level 2 mainly determined by $\tau_{20} \sim 100$ ps gives the possibility to exploit the population inversion beyond the time duration of the pump pulse (here ~10 ps). Projecting the measured trends for losses and population inversion to pump intensity an order of magnitude higher than those reached in the present experiment, we deduce that positive laser gain in the range 2.5−6.0 THz can be achieved in optically pumped quantum wells grown on silicon substrates.

■ ASSOCIATED CONTENT

Supporting Information

The Supporting Information is available free of charge on the ACS Publications website at DOI: 10.1021/acsphotonics.5b00561.

Growth process performed with the CVD technique and the results concerning the sample crystalline quality and the high precision achieved in the heterostructure geometry; calculated band structure including both L and Δ_2 valleys; TEM cross-section images showing the abrupt interfaces and the low defect density along the structure; and single beam traces of THz-TDS and FT-IR providing the estimate of experimental accuracy vs frequency (PDF)

■ AUTHOR INFORMATION

Corresponding Author

*E-mail: michele.ortolani@roma1.infn.it.

Notes

The authors declare no competing financial interest.

■ ACKNOWLEDGMENTS

We thank Peter Michel and the ELBE team for their dedicated support. The research leading to these results has received funding under the 'Research Infrastructure' action of the 'Capacities' Programme, CALIPSO Grant number n.312284.

■ REFERENCES

(1) Helm, M.; England, P.; Colas, E.; DeRosa, F.; Allen, S. J. Intersubband emission from semiconductor superlattices excited by sequential resonant tunneling. *Phys. Rev. Lett.* **1989**, *63*, 74−77.

(2) Smet, J. H.; Fonstad, C. G.; Hu, Q. Intrawell and interwell intersubband transitions in multiple quantum wells for far-infrared sources. *J. Appl. Phys.* **1996**, *79*, 9305−9320.

(3) Helm, M. Intersubband Transitions in Quantum Wells. In *Semiconductors and Semimetals*; Liu, H. C., Capasso, F., Eds.; Academic Press: New York, 2000; pp 1−99.

(4) Williams, B. S. Terahertz quantum-cascade lasers. *Nat. Photonics* **2007**, *1*, 517−525.

(5) Paul, D. J. The progress towards terahertz quantum cascade lasers on silicon substrates. *Laser & Photon. Rev.* **2010**, *4*, 610−632.

(6) Dehlinger, G.; Diehl, L.; Gennser, U.; Sigg, H.; Faist, J.; Ensslin, K.; Grützmacher, D.; Müller, E. Intersubband Electroluminescence from Silicon-Based Quantum Cascade Structures. *Science* **2000**, *290*, 2277−2280.

(7) Lynch, S. A.; Bates, R.; Paul, D. J.; Norris, D. J.; Cullis, A. G.; Ikonić, Z.; Kelsall, R. W.; Harrison, P.; Arnone, D. D.; Pidgeon, C. R. Intersubband electroluminescence from Si/SiGe cascade emitters at terahertz frequencies. *Appl. Phys. Lett.* **2002**, *81*, 1543−1545.

(8) Bates, R.; Lynch, S. A.; Paul, D. J.; Ikonić, Z.; Kelsall, R. W.; Harrison, P.; Liew, S. L.; Norris, D. J.; Cullis, A. G.; Tribe, W. R.; Arnone, D. D. Interwell intersubband electroluminescence from Si/SiGe quantum cascade emitters. *Appl. Phys. Lett.* **2003**, *83*, 4092−4094.

(9) Paul, D. J. Si/SiGe heterostructures: from material and physics to devices and circuits. *Semicond. Sci. Technol.* **2004**, *19*, R75−R108.

(10) Indjin, D.; Ikonić, Z.; Jovanovic, V. D.; Vukmirovic, N.; Harrison, P.; Kelsall, R. W. Relationship between carrier dynamics and temperature in terahertz quantum cascade structures: simulation of GaAs/AlGaAs, SiGe/Si and GaN/AlGaN devices. *Semicond. Sci. Technol.* **2005**, *20*, S237−S245.

(11) Pidgeon, C. R.; Phillips, P. J.; Carder, D.; Murdin, B. N.; Fromherz, T.; Paul, D. J.; Ni, W.-X.; Zhao, M. Pump−probe measurement of lifetime engineering in SiGe quantum wells below the optical phonon energy. *Semicond. Sci. Technol.* **2005**, *20*, L50−L52.

(12) Driscoll, K.; Paiella, R. Design of n -type silicon-based quantum cascade lasers for terahertz light emission. *J. Appl. Phys.* **2007**, *102*, 093103−093103.

(13) Rauter, P.; Fromherz, T.; Vinh, N. Q.; Murdin, B. N.; Phillips, J. P.; Pidgeon, C. R.; Diehl, L.; Dehlinger, G.; Grützmacher, D.; Zhao, M.; Ni, W.-X.; Bauer, G. Direct determination of ultrafast intersubband

DOI: 10.1021/acsphotonics.5b00561
ACS Photonics 2016, 3, 403−414

hole relaxation times in voltage biased SiGe quantum wells by a density matrix interpretation of femtosecond resolved photocurrent experiments. *New J. Phys.* **2007**, *9*, 128−139.
(14) Rauter, P.; Fromherz, T.; Falub, C.; Grützmacher, D.; Bauer, G. SiGe quantum well infrared photodetectors on pseudosubstrate. *Appl. Phys. Lett.* **2009**, *94*, 081115−081115.
(15) Valavanis, A.; Dinh, T. V.; Lever, L. J. M.; Ikonić, Z.; Kelsall, R. W. Material configurations for n-type silicon-based terahertz quantum cascade lasers. *Phys. Rev. B: Condens. Matter Mater. Phys.* **2011**, *83*, 195321.
(16) Sookchoo, P.; Sudradjat, F. F.; Kiefer, A. M.; Durmaz, H.; Paiella, R.; Lagally, M. G. Strain Engineered SiGe Multiple-Quantum-Well Nanomembranes for Far-Infrared Intersubband Device Applications. *ACS Nano* **2013**, *7*, 2326−2334.
(17) Boztug, C.; Sanchez-Pérez, J. R.; Cavallo, F.; Lagally, M. G.; Paiella, R. Strained-Germanium Nanostructures for Infrared Photonics. *ACS Nano* **2014**, *8*, 3136−3151.
(18) Wirths, S.; Geiger, R.; von den Driesch, N.; Mussler, G.; Stoica, T.; Mantl, S.; Ikonić, Z.; Luysberg, M.; Chiussi, S.; Hartmann, J. M.; Sigg, H.; Faist, J.; Buca, D.; Grützmacher, D. Lasing in direct-bandgap GeSn alloy grown on Si. *Nat. Photonics* **2015**, *9*, 88−92.
(19) Faist, J.; Capasso, F.; Sivco, D. L.; Sirtori, C.; Hutchinson, A. L.; Cho, A. Y. Quantum Cascade Laser. *Science* **1994**, *264*, 553−556.
(20) Köhler, R.; Tredicucci, A.; Beltram, F.; Beere, H. E.; Linfield, E. H.; Davies, A. G.; Ritchie, D. A.; Iotti, R. C.; Rossi, F. Terahertz semiconductor-heterostructure laser. *Nature* **2002**, *417*, 156−159.
(21) Liu, H. C.; Cheung, I. W.; SpringThorpe, A. J.; Dharma-wardana, C.; Wasilewski, Z. R.; Lockwood, D. J.; Aers, G. C. Intersubband Raman Laser. *Appl. Phys. Lett.* **2001**, *78*, 3580−3582.
(22) Liu, H. C.; Song, C. Y.; Wasilewski, Z. R.; SpringThorpe, A. J.; Cao, J. C.; Dharma-wardana, C.; Aers, G. C.; Lockwood, D. J.; Gupta, J. A. Coupled Electron-Phonon Modes in Optically Pumped Resonant Intersubband Lasers. *Phys. Rev. Lett.* **2003**, *90*, 077402−077402.
(23) Maung, S. M.; Katayama, S. Gain of intersubband Raman lasing in modulation-doped asymmetric coupled double quantum wells. *Phys. E* **2004**, *21*, 774−778.
(24) Troccoli, M.; Belyanin, A.; Capasso, F.; Cubukcu, E.; Sivco, D. L.; Cho, A. Y. Raman injection laser. *Nature* **2005**, *433*, 845−848.
(25) Scheinert, M.; Sigg, H.; Tsujino, S.; Giovannini, M.; Faist, J. Intersubband Raman laser from Ga In As/Al In As double quantum wells. *Appl. Phys. Lett.* **2007**, *91*, 131108−131108.
(26) Belkin, M. A.; Capasso, F.; Belyanin, A.; Sivco, D. L.; Cho, A. Y.; Oakley, D. C.; Vineis, C. J.; Turner, G. W. Terahertz quantum-cascade-laser source based on intracavity difference-frequency generation. *Nat. Photonics* **2007**, *1* (5), 288−292.
(27) Khurgin, J. B.; Sun, G.; Friedman, L. R.; Soref, A. Comparative analysis of optically pumped intersubband lasers and intersubband Raman oscillators. *J. Appl. Phys.* **1995**, *78*, 7398−7400.
(28) Liu, H. C.; SpringThorpe, A. J. Optically pumped intersubband laser: Resonance positions and many-body effects. *Phys. Rev. B: Condens. Matter Mater. Phys.* **2000**, *61*, 15629−15632.
(29) Lavon, Y.; Sa'ar, A.; Moussa, Z.; Julien, F. H.; Planel, R. Observation of optically pumped midinfrared intersubband luminescence in a coupled quantum wells structure. *Appl. Phys. Lett.* **1995**, *67*, 1984−1986.
(30) Gauthier-Lafaye, O.; Boucaud, P.; Julien, F. H.; Sauvage, S.; Cabaret, S.; Lourtioz, J.-M.; Thierry-Mieg, V.; Planel, R. Long-wavelength (≈15.5 μm) unipolar semiconductor laser in GaAs quantum wells. *Appl. Phys. Lett.* **1997**, *71*, 3619−3621.
(31) Gauthier-Lafaye, O.; Sauvage, S.; Boucaud, P.; Julien, F. H.; Glotin, F.; Prazeres, R.; Ortega, J.-M.; Thierry-Mieg, V.; Planel, R. Investigation of mid-infrared intersubband stimulated gain under optical pumping in GaAs/AlGaAs quantum wells. *J. Appl. Phys.* **1998**, *83*, 2920−2926.
(32) Gauthier-Lafaye, O.; Julien, F. H.; Cabaret, S.; Lourtioz, J.-M.; Strasser, G.; Gornik, E.; Helm, M.; Bois, P. High-power GaAs/AlGaAs quantum fountain unipolar laser emitting at 14.5 μm with 2.5% tenability. *Appl. Phys. Lett.* **1999**, *74*, 1537−1539.
(33) Gauthier-Lafaye, O.; Seguin-Roa, B.; Julien, F. H.; Collot, P.; Sirtori, C.; Duboz, J. Y.; Strasser, G. High-power tunable quantum fountain unipolar lasers. *Phys. E* **2000**, *7*, 12−19.
(34) Vukmirović, N.; Jovanović, V. D.; Indjin, D.; Ikonić, Z.; Harrison, P.; Milanović, V. Optically pumped terahertz laser based on intersubband transitions in a GaN/AlGaN double quantum well. *J. Appl. Phys.* **2005**, *97*, 103106−103106.
(35) Beeler, M.; Trichas, E.; Monroy, E. III-nitride semiconductors for intersubband optoelectronics: a review. *Semicond. Sci. Technol.* **2013**, *28*, 074022−074022.
(36) Califano, M.; Vinh, N. Q.; Phillips, P. J.; Ikonić, Z.; Kelsall, R. W.; Harrison, P.; Pidgeon, C. R.; Murdin, B. N.; Paul, D. J.; Townsend, P.; Zhang, J.; Ross, I. M.; Cullis, A. G. Interwell relaxation times in p-Si/SiGe asymmetric quantum well structures: Role of interface roughness. *Phys. Rev. B: Condens. Matter Mater. Phys.* **2007**, *75*, 045338−045338.
(37) Julien, F. H.; Leburton, J-.P. Infrared Intersubband Emission in Optically Pumped Quantum Wells. In *Long Wavelength Infrared Emitters Based on Quantum Wells and Superlattices*; Helm, M., Ed.; Gordon and Breach Science Publishers: Amsterdam, 2000; pp 89−134.
(38) Carosella, F.; Ndebeka-Bandou, C.; Ferreira, R.; Dupont, E.; Unterrainer, K.; Strasser, G.; Wacker, A.; Bastard, G. Free-carrier absorption in quantum cascade structures. *Phys. Rev. B: Condens. Matter Mater. Phys.* **2012**, *85*, 085310.
(39) Ndebeka-Bandou, C.; Carosella, F.; Ferreira, R.; Bastard, G. Free-carrier absorption in asymmetric double quantum well structures due to static scatterers in the in-plane polarization. *Phys. Rev. B: Condens. Matter Mater. Phys.* **2014**, *89*, 075313.
(40) Capellini, G.; DeSeta, M.; Busby, Y.; Pea, M.; Evangelisti, F.; Nicotra, G.; Spinella, C.; Nardone, M.; Ferrari, C. Strain relaxation in high Ge content SiGe layers deposited on Si. *J. Appl. Phys.* **2010**, *107*, 063504−063504.
(41) DeSeta, M.; Capellini, G.; Busby, Y.; Evangelisti, F.; Ortolani, M.; Virgilio, M.; Grosso, G.; Pizzi, G.; Nucara, A.; Lupi, S. Conduction band intersubband transitions in Ge/SiGe quantum wells. *Appl. Phys. Lett.* **2009**, *95*, 051918−051918.
(42) Pavlov, S. G.; Böttger, U.; Hovenier, J. N.; Abrosimov, N. V.; Riemann, H.; Zhukavin, R.; Kh; Shastin, V. N.; Redlich, B.; van der Meer, A. F. G.; Hübers, H.-W. Stimulated terahertz emission due to electronic Raman scattering in silicon. *Appl. Phys. Lett.* **2009**, *94*, 171112.
(43) Pavlov, S. G.; Böttger, U.; Eichholz, R.; Abrosimov, N. V.; Riemann, H.; Shastin, V. N.; Redlich, B.; Hübers, H.-W. Terahertz lasing from silicon by infrared Raman scattering on bismuth centers. *Appl. Phys. Lett.* **2009**, *95*, 201110.
(44) Ortolani, M.; Stehr, D.; Wagner, M.; Helm, M.; Pizzi, G.; Virgilio, M.; Grosso, G.; Capellini, G.; DeSeta, M. Long intersubband relaxation times in n-type germanium quantum wells. *Appl. Phys. Lett.* **2011**, *99*, 201101−201101.
(45) Barbieri, S.; Ravaro, M.; Gellie, P.; Santarelli, G.; Manquest, C.; Sirtori, C.; Khanna, S. P.; Linfield, E. H.; Davies, A. G. Coherent sampling of active mode-locked terahertz quantum cascade lasers and frequency synthesis. *Nat. Photonics* **2011**, *5*, 306−313.
(46) Tomić, S.; Milanović, V.; Ikonić, Z. Gain Optimization in Optically Pumped AlGaAs Unipolar Quantum-Well Lasers. *IEEE J. Quantum Electron.* **2001**, *37*, 1337−1344.
(47) Virgilio, M.; Ortolani, M.; Teich, M.; Winnerl, S.; Helm, M.; Sabbagh, D.; Capellini, G.; DeSeta, M. Combined effect of electron and lattice temperatures on the long intersubband relaxation times of Ge/Si_xGe_{1-x} quantum wells. *Phys. Rev. B: Condens. Matter Mater. Phys.* **2014**, *89*, 045311.
(48) Williams, B. S.; Xu, B.; Hu, Q.; Melloch, M. R. Narrow-linewidth terahertz intersubband emission from three-level systems. *Appl. Phys. Lett.* **1999**, *75*, 2927−2929.
(49) Virgilio, M.; Bonfanti, M.; Chrastina, D.; Neels, A.; Isella, G.; Grilli, E.; Guzzi, M.; Grosso, G.; Sigg, H.; von Känel, H. Polarization-dependent absorption in Ge/SiGe multiple quantum wells: Theory

DOI: 10.1021/acsphotonics.5b00561
ACS Photonics 2016, 3, 403−414

and experiment. *Phys. Rev. B: Condens. Matter Mater. Phys.* **2009**, *79*, 075323.
(50) Ciasca, G.; DeSeta, M.; Capellini, G.; Evangelisti, F.; Ortolani, M.; Virgilio, M.; Grosso, G.; Nucara, A.; Calvani, P. Terahertz intersubband absorption and conduction band alignment in n-type Si/SiGe multiple quantum wells. *Phys. Rev. B: Condens. Matter Mater. Phys.* **2009**, *79*, 085302.
(51) Busby, Y.; DeSeta, M.; Capellini, G.; Evangelisti, F.; Ortolani, M.; Virgilio, M.; Grosso, G.; Pizzi, G.; Calvani, P.; Lupi, S.; Nardone, M.; Nicotra, G.; Spinella, C. Near- and far-infrared absorption and electronic structure of Ge-SiGe multiple quantum wells. *Phys. Rev. B: Condens. Matter Mater. Phys.* **2010**, *82*, 205317.
(52) DeSeta, M.; Capellini, G.; Ortolani, M.; Virgilio, M.; Grosso, G.; Nicotra, G.; Zaumseil, P. Narrow intersubband transitions in n-type Ge/SiGe multi-quantum wells: control of the terahertz absorption energy trough the temperature dependent depolarization shift. *Nanotechnology* **2012**, *23*, 465708−465708.
(53) Jacoboni, C.; Nava, F.; Canali, C.; Ottaviani, G. Electron drift velocity and diffusivity in germanium. *Phys. Rev. B: Condens. Matter Mater. Phys.* **1981**, *24*, 1014−1026.
(54) Unuma, T.; Yoshita, M.; Noda, T.; Sakaki, H.; Akiyama, H. Intersubband absorption linewidth in GaAs quantum wells due to scattering by interface roughness, phonons, alloy disorder, and impurities. *J. Appl. Phys.* **2003**, *93*, 1586−1597.
(55) Virgilio, M.; Sabbagh, D.; Ortolani, M.; DiGaspare, L.; Capellini, G.; DeSeta, M. Physical mechanisms of intersubband-absorption linewidth broadening in s-Ge/SiGe quantum wells. *Phys. Rev. B: Condens. Matter Mater. Phys.* **2014**, *90*, 155420.
(56) Virgilio, M.; Grosso, G.; Pizzi, G.; DeSeta, M.; Capellini, G.; Ortolani, M. Modeling picosecond electron dynamics of pump-probe intersubband spectroscopy in n-type Ge/SiGe quantum wells. *Phys. Rev. B: Condens. Matter Mater. Phys.* **2012**, *86*, 205317.
(57) Wu, Q.; Zhang, X.-C. 7 terahertz broadband GaP electro-optic sensor. *Appl. Phys. Lett.* **1997**, *70*, 1784−1786.
(58) Casalbuoni, S.; Schlarb, H.; Schmidt, B.; Schmüser, P.; Steffen, B.; Winter, A. Numerical studies on the electro-optic detection of femtosecond electron bunches. *Phys. Rev. Spec. Top.–Accel. Beams* **2008**, *11*, 072802.
(59) Kinsler, P.; Harrison, P.; Kelsall, R. W. Intersubband electron-electron scattering in asymmetric quantum wells designed for far-infrared emission. *Phys. Rev. B: Condens. Matter Mater. Phys.* **1998**, *58*, 4771−4771.
(60) Stehr, D.; Winnerl, S.; Helm, M.; Dekorsy, T.; Roch, T.; Strasser, G. Pump-probe spectroscopy of interminiband relaxation and electron cooling in doped superlattices. *Appl. Phys. Lett.* **2006**, *88*, 151108−151108.
(61) Lobo, R. P. S. M.; LaVeigne, J. D.; Reitze, D. H.; Tanner, D. B.; Barber, H.; Jacques, E.; Bosland, P.; Burns, J.; Carr, G. L. Photoinduced time-resolved electrodynamics of superconducting metals and alloys. *Phys. Rev. B: Condens. Matter Mater. Phys.* **2005**, *72*, 024510.
(62) Dressel, M.; Grüner, G. *Electrodynamics of Solids*; Cambridge University Press: Cambridge, U.K., 2002; pp 9−171.
(63) Liu, A.; Ning, C. Z. Terahertz optical gain based on intersubband transitions in optically pumped semiconductor quantum wells: Coherent pump−probe interactions. *Appl. Phys. Lett.* **1999**, *75*, 1207−1209.
(64) Lynch, S. A.; Townsend, P.; Matmon, G.; Paul, D. J.; Bain, M.; Gamble, H. S.; Zhang, J.; Ikonic, Z.; Kelsall, R. W.; Harrison, P. Temperature dependence of terahertz optical transitions from boron and phosphorus dopant impurities in silicon. *Appl. Phys. Lett.* **2005**, *87*, 101114−8.
(65) Williams, B. J.; Kumar, S.; Callebaut, H.; Hu, Q.; Reno, J. L. Terahertz quantum-cascade laser at lambda 100 mu m using metal waveguide for mode confinement. *Appl. Phys. Lett.* **2003**, *83*, 2124−2127.

DOI: 10.1021/acsphotonics.5b00561
ACS Photonics 2016, 3, 403−414